Pressure reconstruction from PIV measurements in the bow region of a fast ship

Jacobi, G.; Thill, C. H.; Huijsmans, R. H.M.

DOI
10.1016/j.oceaneng.2021.110318

Publication date
2022

Document Version
Final published version

Published in
Ocean Engineering

Ocean Engineering 252 (2022) 110318

Contents lists available at ScienceDirect

Ocean Engineering

journal homepage: www.elsevier.com/locate/oceaneng

Pressure reconstruction from PIV measurements in the bow region of a fast ship

G. Jacobi *, C.H. Thill, R.H.M. Huijsmans

Delft University of Technology, Mekelweg 2, 2628CD Delft, The Netherlands

ARTICLE INFO

Keywords:
Particle image velocimetry
Pressure reconstruction
High-speed-craft

ABSTRACT

The paper presents velocity measurements, using particle image velocimetry, as well as a reconstruction of hydrodynamic pressures for the analysis of fast ships. Stereoscopic PIV measurements with a towed underwater PIV system are conducted during towing tank tests to obtain the velocity field in the bow region of a fast ship at speeds up to Fr=0.8. While the model is kept at a fixed trim and sinkage, multi-plane PIV measurements with a total of 68 measurement planes are conducted to reconstruct a volumetric representation of the time-averaged velocity field in the bow region. The obtained velocity field is subsequently used for a volumetric description of the time-averaged hydrodynamic pressure field. In addition to these captive runs, forced oscillation tests are conducted. During these tests, the flow field is recorded in three successive planes to obtain a local phase-averaged description of the velocity and its gradients for the reconstruction of the phase-averaged hydrodynamic pressure field. The postprocessing procedure for the pressure reconstruction, including the solution of the Poisson equation, is implemented into the open-source CFD package OpenFOAM. For the detection of the free surface and the ship hull, an automated procedure is presented. Experimental results are finally compared to results from numerical simulations. Results show that the PIV method is capable of capturing the flow characteristics in the bow region of a fast ship. In addition, it can be used together with the pressure Poisson equation to obtain the hydrodynamic pressure field. However, large out-of-plane velocities require a large dynamic range, which limits the resolution of local effects close to the ship hull.

1. Introduction

The particle image velocimetry technique (PIV) has been increasingly applied in recent years to measure the flow field in towing tank applications. While the fluid to be investigated is seeded with particles that follow the flow, a laser sheet illuminates the particles in the measurement plane. Their velocity can be determined from the cross-correlation of successive pictures taken with a short time separation (Adrian and Westerweel, 2011). The first application in a towing tank facility is reported by Dong et al. (1997) for the investigation of the bow wave structure of a ship. Further applications include, amongst others, wake flow measurements (Gui et al., 2001; Falchi et al., 2014) and most recently (Capone et al., 2019), and measurements with ship models in waves (Longo et al., 2001, 2007; Huijsmans et al., 2005). With the Navier–Stokes equations describing the relationship between the measured flow field and the pressure field, it has been shown that the obtained velocities and velocity gradients can be also utilized for a reconstruction of the pressure field (van Oudheusden, 2013). The pressure-PIV technique is well studied and widely accepted in the field of aero- and fluid-dynamics. The recent development of the PIV technique and hardware components allow for a reconstruction of volumetric and even time-resolved pressure fields, using tomographic PIV (Schneiders et al., 2016) or stereoscopic multi-plane PIV (Ragni et al., 2012). An overview of the most common methods and a comparison of their performance is given by van Gent et al. (2017). A more detailed discussion of the reconstruction of pressures from PIV measurements is given in Section 6. In the field of ship hydrodynamics, the technique has been first successfully applied by Nila et al. (2013) for the estimation of slamming loads during the water entry of rigid bodies from planar PIV measurements. A first application of the pressure-PIV technique during towing tank tests has been reported by Jacobi et al. (2019). Here, the flow field and the resulting hydrodynamic pressure distribution in the transom region of a fast ship have been assessed with stereoscopic multi-plane PIV measurements. While the transom was equipped with an interceptor, the influence of different interceptor heights and ship speeds on the three-dimensional pressure field could be obtained. Results from these tests showed that the pressure PIV technique can be applied for the reconstruction of hydrodynamic pressures in the flow field around a fast ship. It was focused on testing the overall feasibility

* Corresponding author.
E-mail address: g.jacobi@tudelft.nl (G. Jacobi).

https://doi.org/10.1016/j.oceaneng.2021.110318
Received 3 March 2020; Received in revised form 29 November 2021; Accepted 2 December 2021
Available online 8 April 2022

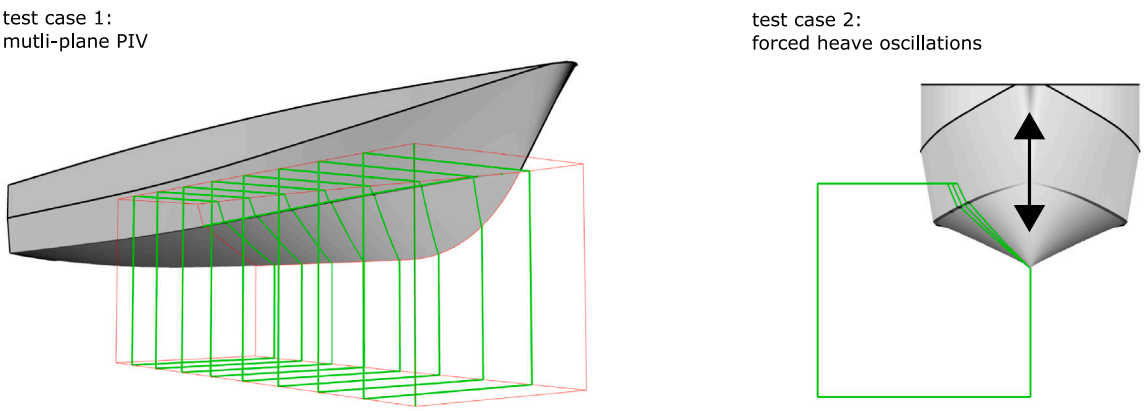

Fig. 1. Schematic description of the test cases: 1. Reconstruction of the time-averaged volumetric flow field from multi-plane PIV measurements (left). 2. Measurement of the phase-averaged flow field during forced oscillation tests (right).

of the method at high towing tank carriage velocities and the assessment of structural vibrations of the carriage that influence the quality of the measurements. For this purpose, the model of a generic planing hull was chosen with no geometrical variations within the measurement plane. However, ships mostly have complex hull geometries, and thus identification of these is necessary for a successful velocity and pressure field measurement. Accurate feature identification and masking is not only necessary for an improved correlation close to features such as the ship hull and the water surface, but is also key for a correct application of boundary conditions for the solution of the pressure Poisson Equation. Especially when the position of objects and interfaces changes, it may be due to the change of the measurement position or an unsteady characteristic of the observed flow, an automated procedure is necessary. Furthermore, during the measurements presented by Jacobi et al. (2019), the measurement plane was aligned with the main flow direction, resulting in comparatively large in-plane velocity components. While this is considered to be ideal, in towing tank applications the measurement plane often has to be perpendicular to the flow to capture the main features of certain flow structures such as vortices. It has been shown in Adrian and Westerweel (2011) that the out-of-plane component can have a significant influence on the correlation peak quality. A perpendicular alignment of the measurement plane with the main flow direction becomes even more critical when in-plane velocity components are small compared to the out-of-plane components, which for towed PIV systems are mostly dominated by the carriage speed. Especially at high carriage velocities, an orientation of the measurement plane perpendicular to the main flow direction is thus considered as critical. Both of the previously addressed topics are discussed in this paper in the context of a practical application. PIV measurements of the flow in the bow region of a fast-displacement vessel and subsequently a reconstruction of the pressure field from these are presented for a steady captive model, in addition to results obtained with a model undergoing forced heave oscillations.

2. Test case

The vessel investigated in this study is a conceptual design of the Enlarged Ship Concept developed by Keuning et al. (2001). With its V-shaped hull, it represents a typical fast-displacement vessel. PIV measurements are conducted in the bow region of this model to capture the local flow and reconstruct the hydrodynamic pressure field in this region. Next to calm water tests with a model at fixed trim and sinkage, forced heave oscillations are performed (see Fig. 1). For the calm water tests, a model speed of Fr=0.8 is selected. This is equal to 37 kn in full-scale and 3.32 m/s at the selected model scale. The flow field is obtained over a length of 0.68 m in the bow region of the model by conducting multi-plane PIV measurements. Using the ship coordinate system as a reference, measurements started at x=1.2 m in front of the transom. With a spacing of the measurement planes of 0.01 m, the time-averaged flow field will be obtained by acquiring the flow field in a total of 68 measurement planes in order to reconstruct a volumetric description of the flow field in this area. Using this velocity field, the hydrodynamic pressure distributions in the flow field and on the ship hull are calculated by solving the Poisson equation. During the forced oscillation tests the flow field is recorded in three successive planes which are perpendicular to the flow direction to obtain all necessary velocity components and their derivatives to reconstruct the phase-averaged pressure field. The model oscillates at a frequency of 1 Hz. This is comparable to the lower end of the wave encounter frequency range selected by De Jong (2011) during tests in regular waves with the same model. As the PIV system acquisition frequency is limited to 50 Hz (see Section 3), no higher oscillation frequencies are chosen to guarantee a sufficiently small time-step. The model oscillates with an amplitude 0.5 times the draft of the model. The longitudinal position of the measurement plane is at x=1.35 m.

3. Experimental setup

The towing tank experiments were carried out in the large towing tank of the ship hydrodynamics laboratory of TU Delft. Both calm water tests with the captive model, as well as forced heave oscillations, are conducted with the same setup. An overview of the setup is given in Figs. 2 and 3, which show the ship model mounted to a hexapod next to the stereo-PIV system. The hexapod is used to accurately position the model within the field of view of the PIV system and set the model to its correct running trim and sinkage. To increase the stiffness of the stereo-PIV system, no traversing system is used to change the measurement plane position during the multi-plane PIV measurements in calm water. Instead, the hexapod is used to reposition the model during the test runs. During the forced oscillation tests, the hexapod is used to perform the forced heave oscillations.

To record the flow field, an underwater stereoscopic PIV system is used with both camera sections fitted within a single torpedo (see Fig. 4). The laser beam is guided below the water surface through a separate strut, where it leaves the strut through a cylindrical lens, forming the light-sheet, which is oriented perpendicular to the towing direction of the carriage. Both cameras are looking at the measurement area through a water-filled mirror section, with mirror angles being tilted 120 degrees with respect to the camera viewing direction. This symmetric arrangement with one camera on either side of the light sheet is used to accomplish the highest accuracy during the determination of the out-of-plane velocity component. According to Lawson and Wu (1997), the ratio of the out-of-plane error $\sigma_{\Delta z}$ to the in-plane error $\sigma_{\Delta x}$ for this viewing angle is approximately 1.7. The torpedo, which

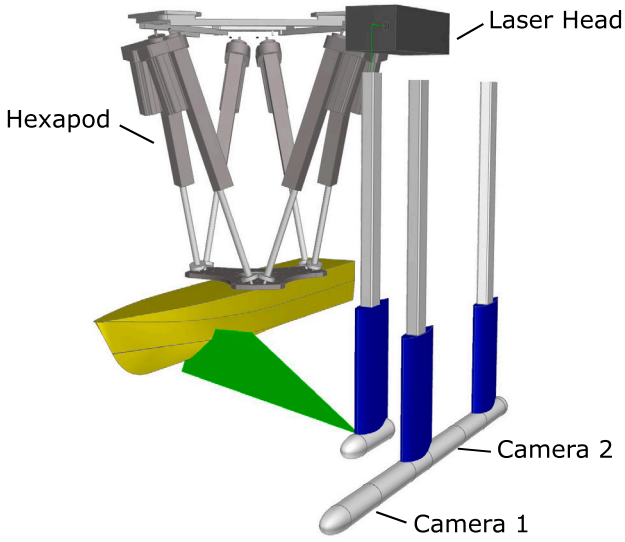

Fig. 2. Schematic overview of experimental setup.

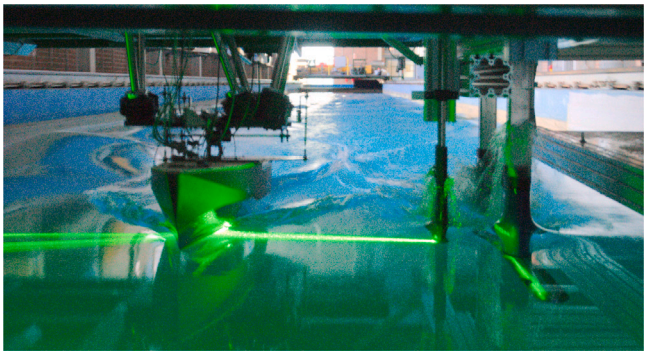

Fig. 3. Photograph of experimental setup.

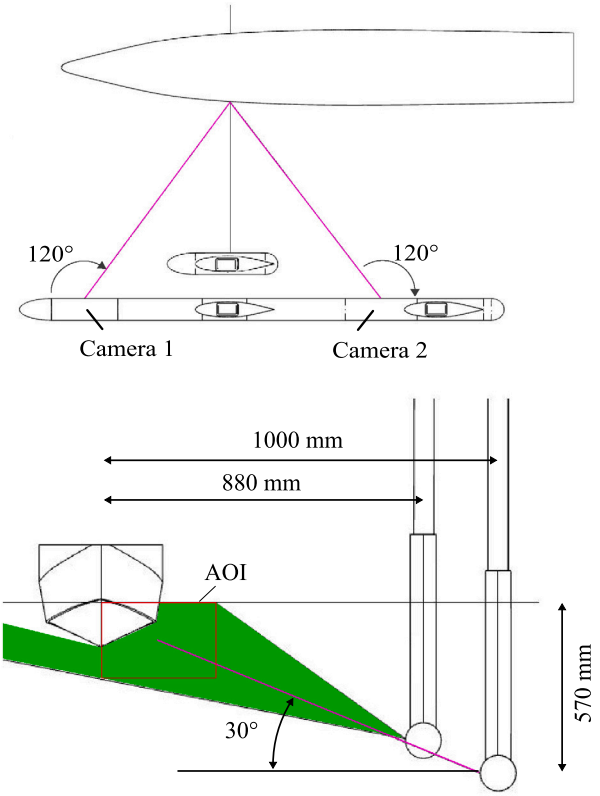

Fig. 4. Schematic description of the optical setup.

accommodates the camera system, has a horizontal stand-off distance of 1000 mm and is submerged 570 mm below the water surface. The camera sections are rotated by 30 degrees around the longitudinal axis of the torpedo to look upwards at the measurement area. This enables a better view of the flow within the region of the bow wave. The measurement plane is illuminated with a Litron Nano PIV Nd:YAG laser with an energy of 50 mJ/pulse at a wavelength of 532 nm. The laser has two cavities with each having a maximum repetition rate of 50 Hz. For image acquisition, two LaVision Imager MX 4M cameras with a sensor size of 2048 x 2048 pixels and 10-bit color depth are used. The cameras have a pixel size of 5.5 x 5.5 μmm^2 and are equipped with lenses of 28 mm focal length. This results in a field of view of approximately 350 x 450 mm^2 with a digital resolution of approximately 7 x 7 pixels/mm^2. The final area of interest, used for processing the images was limited to a region of 250 x 250 mm^2. As the viewing direction of the cameras is not perpendicular to the measurement plane, a Scheimpflug-adaptor is placed in front of the cameras to keep particles focused over the whole field of view.

Calibration of the cameras is done with a 320 x 320 mm^2 two-level double-sided 3d calibration plate which is carefully aligned in an iterative process perpendicular to the moving direction of the carriage. To guarantee uniform distribution of the 50 μm polymer (Vestosint) particles in the measurement area, a retractable seeding rake is mounted in front of the carriage. After every measurement run the tank is reseeded and a waiting time of 25 min allowed the water to settle in between runs. The data acquisition is done using the commercial software package DaVis 8.4.0 from LaVision. Aiming at 400 vector images per measurement plane for the multi-plane scanning measurements, due to the image acquisition frequency of 50 Hz, velocity fields can be obtained in multiple planes within a single run. Taking into account the acceleration and deceleration phase of the carriage, the flow field is measured in up to three planes at Fr 0.8. To guarantee a high temporal accuracy for the determination of the phase-averaged velocity field during forced oscillation tests, the PIV system is triggered at the beginning of every oscillation cycle to start a recording at 50 Hz. The last three frames in every oscillation cycle have to be omitted, to reset the trigger. At the carriage speed of 2.54 m/s, 38 oscillation cycles are recorded per run.

4. PIV image processing

Before calculating the vector field from the recorded images, the free surface and the ship hull need to be identified in the images. This is necessary for an accurate vector calculation close to the boundaries and an accurate description of the boundaries for the correct application of boundary conditions during pressure reconstruction from the velocity fields. Fig. 5 shows two examples of raw images taken during the multiplane measurements at x=1.4 m and x=1.2 m, transformed to the ship coordinate system using the parameters obtained from the initial calibration. In both pictures, the ship hull can be identified due to the high-intensity reflections of the laser sheet. The free surface, however, is hardly recognizable in both pictures and its position and shape are difficult to obtain from these single images. The position of the free surface can only be guessed from particle agglomerations and disturbances of the free surface due to wave breaking. For this reason, the identification of the free surface and the ship hull is looked at separately. Image processing and feature identification are performed within the MATLAB toolbox.

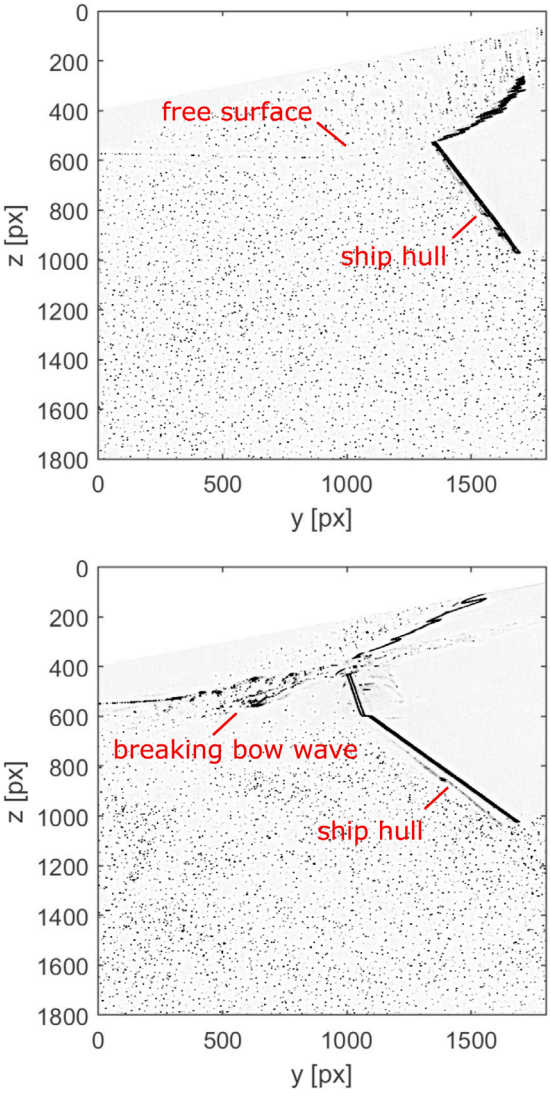

Fig. 5. PIV raw images taken during the multi-plane measurement runs at x=1.3 m and x=1.5 m.

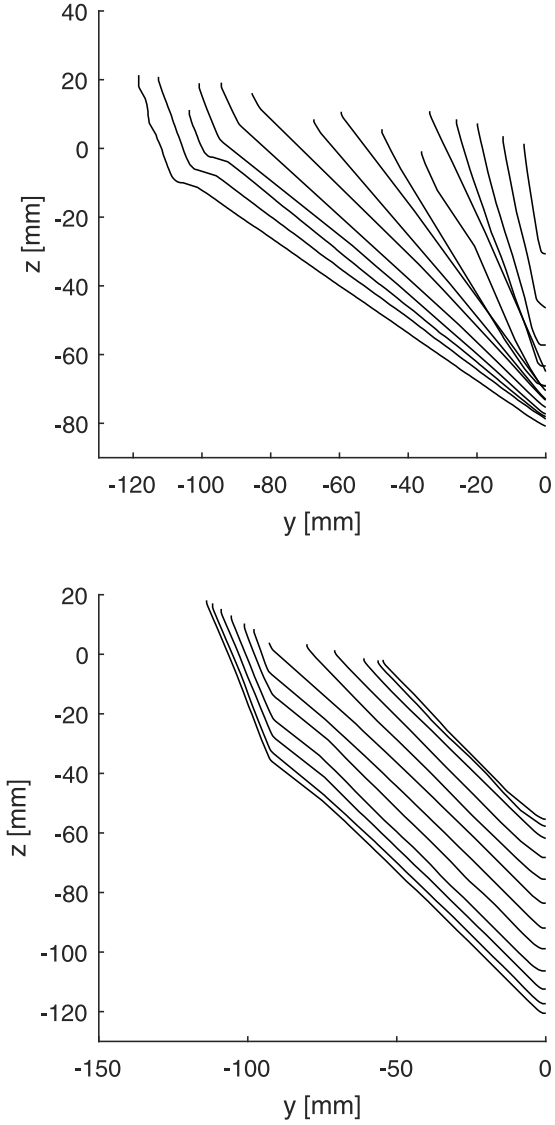

Fig. 6. Selected identified ship hull sections: multi-plane measurements (top), oscillation tests (bottom).

4.1. Ship hull identification

4.1.1. Image filtering and thresholding

As being interested in the detection of the high-intensity reflections on the ship hull, initially, the PIV particles have to be removed from the images. The removal of small objects is done by morphologically opening the images with a 3 × 3 structure element. To account for small variations in the outline of the reflections on the ship hull that are due to small changes in intensity, the image is morphologically closed with a 3 × 3 structure element to fill small holes in the foreground of the picture. To apply the final feature detection, the image needs to be binarized. The threshold level for this is automatically chosen by using Otsu's method (Otsu, 1979). To additionally remove spurious elements from the image and smooth the contour of the reflections on the hull the images are again morphologically opened and subsequently closed.

4.1.2. Feature identification

The final feature identification and extraction step makes use of the fact that the ship hull has a wedge-like shape, visible as a single or a combination of straight lines in the image. Within the field of digital image processing, a well-known technique for the extraction of features and especially lines is the Hough transform (Duda and Hart, 1971). The lower boundary of the object is finally extracted with a moving-maximum filter for masking the image. Fig. 6 shows the identified ship hull for the multi-plane and forced oscillation tests. Following selection of the range of deadrise angles before the identification procedure, the procedure automatically identifies the outline of the ship hull within this range. Furthermore, the procedure is capable of identifying objects that consist of multiple connected straight lines, as seen from sections with submerged chine.

4.2. Free-surface identification

4.2.1. Temporal filtering

As initially stated, the free surface is difficult to identify from a single picture. However, from close inspection of Fig. 5, the position of the free surface can be estimated due to small particle agglomerations in this area and small areas of high intensity from air entrainment due to the breaking bow wave. In order to improve the visibility of the free surface in the images, a temporal filtering procedure is introduced. Due to the change in particle position between images, the images are binned in groups of 10 pictures. Images of every group are then added on top of each other, to increase the number of particle agglomerations

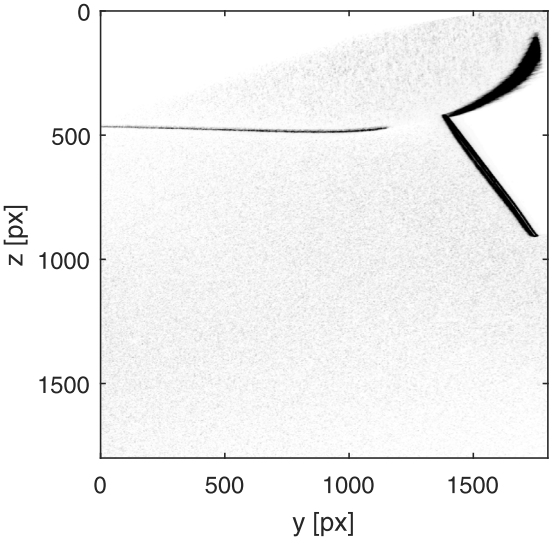

Fig. 7. Time filtered PIV image at x=1.5 m.

at the surface. Isolated PIV particles are removed by morphologically opening the image. The final images, as seen in Fig. 7, are the sum of all bins, which are morphologically closed to remove local variations of intensity. Compared to the initial images, the free surface, as well as the region of the disturbance of the free surface due to the breaking bow wave, can now be identified.

4.2.2. Piecewise surface detection

For the final extraction of the free surface and its lower boundary, the image is masked with the identified ship hull. As already applied for the ship hull identification, Otsu's method is used to binarize the image and to guarantee a fully automatized identification of the free surface. However, the application of Otsu's method to the entire picture does not give satisfying results, due to variations of intensities in the background and the free surface itself. To overcome this problem, a piecewise surface identification procedure is introduced, which considers a local threshold within a certain window. The steps of the procedure are shown in Fig. 8 (top). The method starts the identification at the image boundary and moves along the free surface towards the ship. The starting point for the initial window is chosen from the still water position during the calibration procedure. Within the initial window, the local threshold is determined and the free surface is approximated with a line, determined by a Hough transform. In case the approximation is successful, the outline of the free surface is determined. The detected line is used to predict the location of the next segment, where the previously described procedure is repeated. If no line can be detected within a window, the line detection stops. With this procedure, an approximation of the free surface outline is specified (Fig. 8 (center)). In the final step, a new threshold is calculated for the area within the specified outline, which enables a better approximation of the lower boundary of the surface. The result of the procedure is shown in Fig. 8 (bottom). Given that the proposed method is based on a line detection, the method is limited by the magnitude of the free surface disturbances.

5. Vector field calculation and data reduction

After the application of the individual masks to each image, the calculation of the velocity vector field is completed in multiple correlation iterations using the software package DaVis 8.4. Starting with an interrogation window of 64 x 64 pixels in the initial pass, the window size is iteratively decreased to 24 x 24 pixels. The windows are

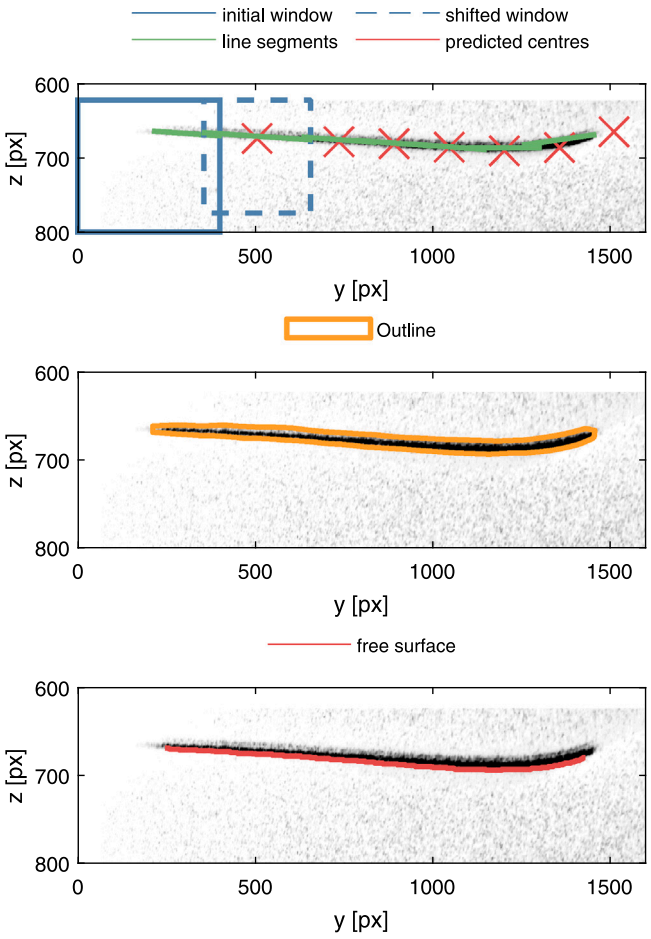

Fig. 8. Free-surface identification procedure (top) and final identified lower edge of free-surface (bottom) at x=1.5 m.

overlapping by 75% and a Gaussian weighting function is used. As the ultimate interest is in the mean value and other statistical properties of the flow, robust outlier detection is needed in between passes, as already a small number of false vectors can significantly change the final result. For this reason, in between passes, a 4-pass regional median filter is used to reject groups of spurious vectors. This type of robust outlier detection is well suited to remove most of the outliers, although with the drawback that some good vectors might also be rejected. Fig. 9 shows an example of the out-of-plane and in-plane velocity components of the mean velocity field which is obtained from 400 vector images. A convergence analysis of the temporal mean for the three velocity components is performed. For sample sizes larger than 200 the residual is of the order magnitude of $10e^{-4}$.

5.1. Multi-plane measurements

For further processing of the multi-plane measurements, the time-averaged velocity fields of all measurement planes are combined to a discrete description of the volumetric velocity field. For this purpose, the velocity field data is converted to a numerical regular grid, which can be handled by the open-source code OpenFOAM. The grid spacing in the longitudinal direction of the ship is 10 mm and equal to the original spacing of the PIV measurement planes. The grid spacing along the y- and z-axis is 0.0018 m, resulting in a total grid size of approximately 10^6 cells. With the information from the masking procedure, the outer surface of the domain is split into separate patches. As the volumetric description of the flow field is obtained from planar measurements, small discontinuities are expected in between these

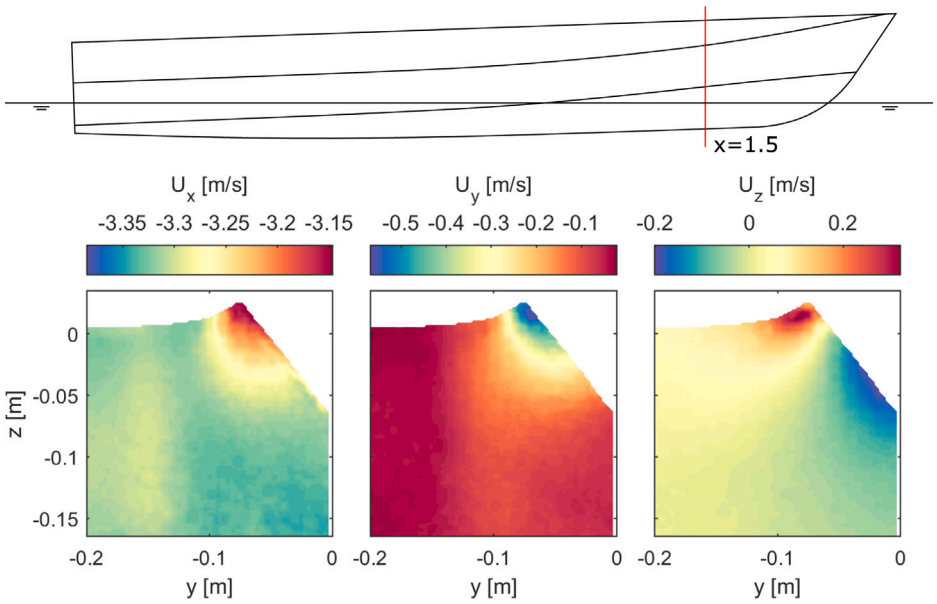

Fig. 9. Time averaged velocity field components at x=1.5 m.

planes. To guarantee, that the reconstructed volumetric velocity field is divergence-free, the divergence-free correction scheme (DCS), which was first proposed by De Silva et al. (2013), is used for smoothing the velocity field. The approach is based on the solution of a constrained minimization problem. The objective is to minimize the difference in kinetic energy between the velocity fields from PIV measurements u_{PIV} and their corrected field u_{corr} with the additional constraint, that the corrected velocity field is divergence-free:

$$\min_{u_{corr}} \frac{1}{m} \sum_{i=1}^{m} \left[\sum_{j=1}^{3} \left(u^i_{corr,j} - u^i_{PIV,j} \right)^2 \right] \quad \text{, with} \tag{1}$$

$$\nabla \cdot u_{corr} = 0 \tag{2}$$

As described by Azijli et al. (2016), the minimization problem can be reformulated to a quadratic programming problem with linear equality constraints. With the measurement data format already being converted to the OpenFOAM data format, the minimization problem is also solved within this toolbox as an optional pre-processing step prior to the solution of the pressure equation.

5.2. Oscillation tests

The acquisition of images during the oscillation tests is synchronized with the motion of the hexapod and each oscillation cycle is stored in a separate data set with each image associated with a fixed phase angle. For each condition 38 oscillation cycles are obtained per carriage run, giving a total of 190 cycles recorded in three consecutive measurement planes. As additional time is needed to reset the trigger for the cycles, at a recording rate of 50 Hz, the phase-averaged velocity fields are be obtained for 47 phase angles. For the determination of the phase-averaged pressure field during the forced oscillation tests, it is necessary to account for the complete material acceleration, this includes, in addition to the convective term, the time derivative of the velocity field. Due to the phase-averaged manner in which the velocity field is obtained, it is expected that the time signal of the velocity field is not smooth and the noise from the phase-averaged velocity fields ultimately affects the quality of the temporal derivative. For a reduction of noise in the derived accelerations, the velocity field is smoothed by performing a piecewise second-order polynomial regression in between time steps, using a Savitzky–Golay filter (Savitzky and Golay, 1964).

6. Pressure reconstruction

Having obtained the velocity fields with the PIV technique, the relation of the measured velocities, their spatial and temporal derivatives, and the pressure gradient is given by the Navier–Stokes equation. Under the assumption that the flow is incompressible, the divergence-free condition holds, i.e., $\nabla \cdot u = 0$ and the pressure gradient can be described as:

$$\frac{\partial p}{\partial x_i} = \rho \left(-\frac{\partial u_i}{\partial t} - u_j \frac{\partial u_i}{\partial x_j} + \nu \frac{\partial^2 u_i}{\partial x_j \partial x_j} \right) \tag{3}$$

As found by De Kat et al. (2009), Koschatzky et al. (2010) and Haigermoser (2009), the contribution of the viscous term can be neglected for Reynolds numbers larger than $Re > 10^3$, leaving the material derivative

$$\frac{D}{Dt} = \rho \left(\frac{\partial u_i}{\partial t} + u_j \frac{\partial u_i}{\partial x_j} \right) \tag{4}$$

as the terms which are mainly contributing to the determination of the pressure field. Several methods have been developed for the determination of the material derivative and depending on the reference frame they can be split up into Lagrangian (material acceleration) and Eulerian methods (local acceleration and convective term). A comprehensive overview of these is given in Wang et al. (2017). While truly Lagrangian methods rely on the tracking of particles, these methods ask for a time resolved acquisition of the 3D velocity field, which can be established with methods such as tomographic particle tracking velocimetry (PTV) or the recently developed shake the box technique (Schanz et al., 2013). In contrast to the truly Lagrangian methods, the Pseudo Lagrangian methods can overcome these limitations by tracking imaginary particles in a series of particle images or velocity fields (Liu and Katz, 2006). Especially when making use of larger time traces, these

methods become more accurate (Pröbsting et al., 2013). Jensen and Pedersen (2004) compared the pseudo Lagrangian method to the basic Euler method, where the local acceleration and convective term are determined separately. When the velocity field could not be determined in a phase- or time-averaged manner they concluded, that the pseudo Lagrangian method is superior to the basic Euler method. However, as the velocity field in the current study is supposed to be stationary during the captive model tests and phase-averaged from the oscillation tests, the basic Euler method is chosen in this study due to its simplicity.

For the reconstruction of the pressure field, Eq. (3) has to be integrated. Starting from a single point, or area, where the reference pressure is known, the pressure field can be found through spatial marching, as first proposed by Baur (1999). To further reduce the accumulation of errors during spatial integration, different marching schemes have been proposed. Van Oudheusden, B.W. (2007) introduced a generalized spatial marching technique based on the field erosion principle. Liu and Katz 2006 proposed an omnidirectional integration method which was later improved due the introduction of a virtual boundary (Liu and Katz, 2011; Haigermoser, 2009).

As an alternative to the integration of the pressure gradient, one can apply the divergence operator to the momentum Eq. (3).

$$\frac{\partial}{\partial x_i}\left(\frac{\partial p}{\partial x_i}\right) = \rho\frac{\partial}{\partial x_i}\left(-\frac{\partial u_i}{\partial t} - u_j\frac{\partial u_i}{\partial x_j} + \nu\frac{\partial^2 u_i}{\partial x_j \partial x_j}\right) \tag{5}$$

This results in a Poisson equation, which can be solved with the help of appropriate boundary conditions. Under consideration of the divergence-free condition $\nabla \cdot u = 0$, the local acceleration and the viscous term disappear and the pressure Poisson equation further reduces to:

$$\frac{\partial^2 p}{\partial x_i^2} = -\rho\frac{\partial}{\partial x_i}\left(u_j\frac{\partial u_i}{\partial x_j}\right) \tag{6}$$

The disappearance of the acceleration and viscous term does not mean that their influence is neglected, as they will still be present in the boundary conditions, of either Dirichlet or Neumann type. The latter condition is obtained from the momentum Eq. (3) to prescribe the non-homogeneous pressure gradient at the boundary of the measurement area:

$$n_i \cdot \frac{\partial p}{\partial x_i} = -\rho n_i \cdot \left(\frac{\partial u_i}{\partial t} + u_j\frac{\partial u_i}{\partial x_j} - \nu\frac{\partial^2 u_i}{\partial x_j \partial x_j}\right) \tag{7}$$

with n_i being the normal vector of the domain boundary. Dirichlet type boundary conditions can be applied at boundaries, where the pressure is known. This can be the pressure of the undisturbed flow or even a reference pressure obtained from additional measurements.

The performance of both methods, the direct integration and the solution of the Poisson equation, has been compared by several authors. A summary of the advantages and disadvantages of both methods is given by van Oudheusden (2013) and van Gent et al. (2017). The performance of both methods often depends on the case of application, however, it is often reported that due to the accumulative error of the spatial marching scheme, the direct integration is more sensitive to measurement noise (Albrecht et al., 2012). For this reason in this study, the Poisson approach has been chosen for the reconstruction of the pressure field.

Due to the time- and phase-averaged character of the measurements, Eq. (6) has to be extended by the Reynolds stress tensor, resulting in a modified Poisson equation for the time- and phase averaged pressure:

$$\frac{\partial^2 \overline{p}}{\partial x_i^2} = -\rho\frac{\partial}{\partial x_i}\left(\overline{u}_j\frac{\partial \overline{u}_i}{\partial x_j} + \frac{\partial \overline{u_i' u_j'}}{\partial x_j}\right) \tag{8}$$

Depending on the case of application, the overbar describes the time- or phase-averaged values obtained from the measurements. Accordingly, the Dirichlet boundary condition changes to

$$n_i \cdot \frac{\partial \overline{p}}{\partial x_i} = -\rho n_i \cdot \left(\frac{\partial \overline{u}_i}{\partial t} + \overline{u}_j\frac{\partial \overline{u}_i}{\partial x_j} - \nu\frac{\partial^2 \overline{u}_i}{\partial x_j \partial x_j} + \frac{\partial \overline{u_i' u_j'}}{\partial x_j}\right) \tag{9}$$

Table 1
Comparison of bias, errors and uncertainties from uniform flow tests for the different velocity components.

Vel. [m/s]	Comp.	Mean [px]	Bias [px]	Error std. dev. [px]	Uncertainty RMS [px]
3.32	x	5.68	0.04	0.16	0.12
0	y	0.06	0.06	0.23	0.17
0	z	0.07	0.077	0.15	0.075

The temporal derivative of the velocity field is only included for the phase-averaged oscillation tests. The calculation of the temporal, as well as spatial derivatives, is obtained with central differences from the spatially smoothed velocity field. The Reynolds stresses are found from variances and covariances of the velocities. The Poisson equation is discretized with the finite-volume method and solved with the open-source package OpenFOAM as described in Jacobi et al. (2019). A similar implementation in OpenFOAM has been already presented by Regert et al. (2011) for a two-dimensional flow field. Recently Felis-Carrasco et al. (2021) presented an approach where the OpenFOAM mesh generator *snappyHexMesh* was applied to improve the numerical grid close to the surface of a submerged cylinder.

Having identified the ship hull and the free surface during the feature identification procedure allows for the application of different boundary conditions on these patches. While the pressure on the water surface is equal to the atmospheric pressure $p = p_a$, a Dirichlet boundary condition is imposed on the free surface patch, for both, the scanning tests as well as the oscillation tests. Due to the symmetry of the ship model and the flow field with respect to the center plane of the ship model, a symmetry boundary condition is imposed, which sets the patch normal components to zero. For the remaining patches, Eq. (9) is used to specify, the pressure gradient in the patch's normal direction. The velocity and acceleration values of the moving ship hull are obtained from the hexapod signal.

Fig. 10 gives a first impression of the reconstructed pressure field in the vicinity of the ship model. The pressure field is reconstructed from the volumetric description of the velocity field, which is obtained from multi-plane PIV measurements. Results are presented at three selected slices perpendicular to the moving direction of the ship model. At all displayed positions, a clear high-pressure region is found in the spray root. The size of this high-pressure region and the peak pressure is increasing by shifting the measurement plane towards the aft of the ship. In measurement plane x_1, the chine of the ship is within the spray root of the bow wave, leading to the highest pressure increase in this region. The limited optical access prevents a full determination of the pressure field within the jet region, which is formed on the ship hull within the bow wave. However, the spray root, where the highest pressure is expected, is well captured in all measurement planes.

7. Measurement uncertainty assessment and propagation

Before velocity fields from PIV measurements and the reconstructed pressure fields are compared to numerical results, a brief discussion of the uncertainty of the obtained velocity fields is given. Further, it is investigated how these influence the final pressure field. While ultimately being interested in the statistical quantities of the measured velocities, the following discussion mostly focuses on the random errors, which are typically dominant due to the finite sample size. For an initial judgment of the random uncertainty components and the bias due to misalignment of the laser sheet with the towing tank coordinate system uniform flow measurements are performed in absence of the test geometry. Concerning the uniform flow measurement in which the flow speed is equal to the carriage speed, only an out-of-plane velocity component is expected with no in-plane velocities. Table 1 shows the main results from the uniform flow measurements at a towing tank carriage velocity of 3.32 m/s. In addition to the statistical quantities,

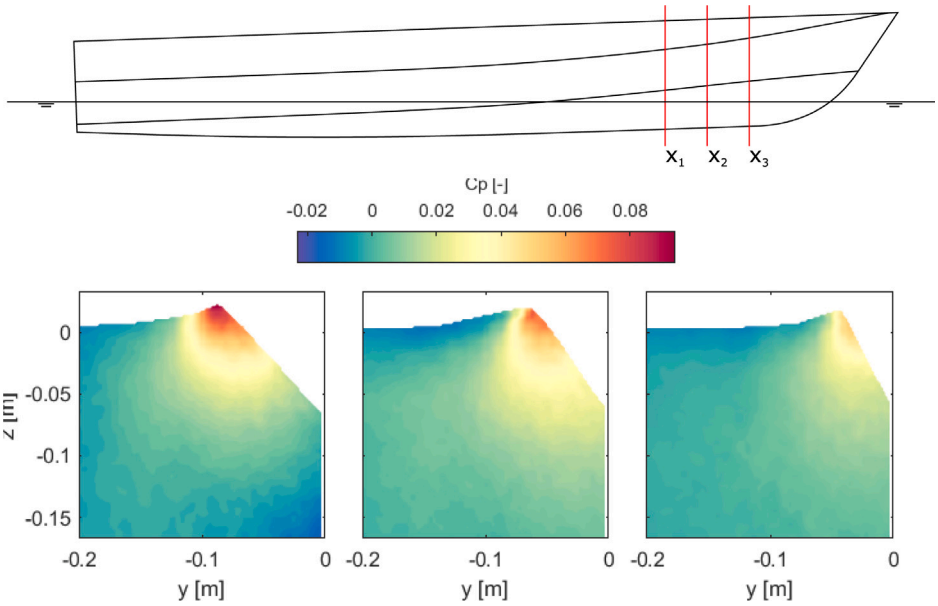

Fig. 10. Example of the reconstructed time-averaged pressure fields at x=1.4 m, x=1.5 m and x=1.6 m.

the root-mean-square (RMS) of the random uncertainties, assessed with the correlation statistics method of Wieneke (2015), are shown for comparison with the standard deviation of the measured velocities. By looking at the out-of-plane velocity component and its equivalent pixel displacement, it has to be noted that the pulse-separation Δt and thus the particle displacement was limited by the light sheet thickness. To prevent any out-of-plane particle loss, particle displacement is one-quarter of the light sheet thickness (Adrian and Westerweel, 2011). Especially in the case of high carriage velocities, the large dynamic range results in a lower resolution. The bias of all three velocity components has a maximum value of 0.07 pixels, while the standard deviation varies between 0.15 and 0.16 pixels for the x and z-component and 0.23 pixels for the y-component. The same trend is reproduced by the RMS values of the uncertainties obtained with the correlation statistics method. The larger standard deviation and RMS uncertainties in the y-direction indicate a slightly stretched correlation peak in this direction. The reason for this can be found in the thickness of the light sheet, which is increased to a maximum to increase the pulse separation Δt. As the particle images of both cameras cannot match perfectly due to the finite thickness of the light sheet, the correlation peak is stretched along the axis spanned by the viewing axes of both cameras. Under the assumption of perfectly still water during the uniform flow measurements, the standard deviation of the measured velocities should match the RMS of the estimated uncertainties. While the trend is well reproduced, with the highest uncertainty being in the y-direction, all uncertainties, determined with the correlation statistics method, are slightly lower. An explanation for this difference might be the fact that the assumption of perfectly still water does not completely hold. As the measurement area is seeded with the help of a seeding rake prior to every run, small fluctuations might still be present, even after a waiting period of 25 min.

The uncertainties obtained from uniform flow measurements, only give an initial indication of the bias and random errors. They do not take into account that due to local flow characteristics the uncertainty during the real measurement can significantly differ from those obtained in uniform flow measurements. Furthermore, any influence of reflections from the model which influences the correlation quality is not taken into account. Fig. 11 shows the RMS uncertainty obtained with the correlation statistics method from a total of 400 images.

It is seen that the uncertainty, obtained from the uniform flow measurements, can only be matched further away from the ship model. While the ship is painted mat black to minimize any reflections, these could not be completely removed. The laser sheet is reflected from the ship model and influences the quality of the correlation peak within this region. While the ship model has a curved surface, it might occur that the reflected light sheet is not aligned with the incoming light sheet and thus affects the quality of the correlation peak. The highest values of uncertainties can be found next to the ship hull and the free surface, exceeding the initially determined uncertainties from the uniform flow measurements by a factor of three.

7.1. Uncertainty propagation

Our focus being the time- and phase-averaged properties of the flow quantities, the uncertainties of the instantaneous velocity fields need to be propagated to those quantities. The uncertainties of the mean velocities and Reynolds stresses are determined according to Sciacchitano and Wieneke (2016). Having obtained the instantaneous uncertainties with the correlation statistics method, the Reynolds normal stresses are again corrected by subtracting the mean-square of these. The final propagation of the uncertainties of the mean velocities and the Reynolds stresses towards the uncertainty of the pressure field is done with Monte Carlo simulations. For a reliable determination of the pressure uncertainty, a total of 10.000 realizations is done. Fig. 12 shows the uncertainties of the mean velocity field magnitude $U_{\overline{|u|}}$ (left) and the result of the uncertainty propagation towards the final pressure field U_{C_p} (right).

Both uncertainty distributions are presented with a confidence interval of 95%. The highest uncertainties can be found close to the ship hull, with maximum values within the spray root of the bow wave. In the far-field, the expanded uncertainty of the time-averaged velocity is approximately $5 \cdot 10^{-3}$ m/s, which is equal to 0.15% of the carriage velocity. The value increases to $3 \cdot 10^{-2}$ m/s in the spray root, which is equal to 1% of the carriage velocity. A similar uncertainty distribution can be found for the expanded uncertainty of the pressure coefficient, which is approximately $6 \cdot 10^{-4}$ in the far-field and $6 \cdot 10^{-3}$ close to the ship hull. The reported values are equal to 0.5% and 5.5% of the peak pressure, detected in the spray root.

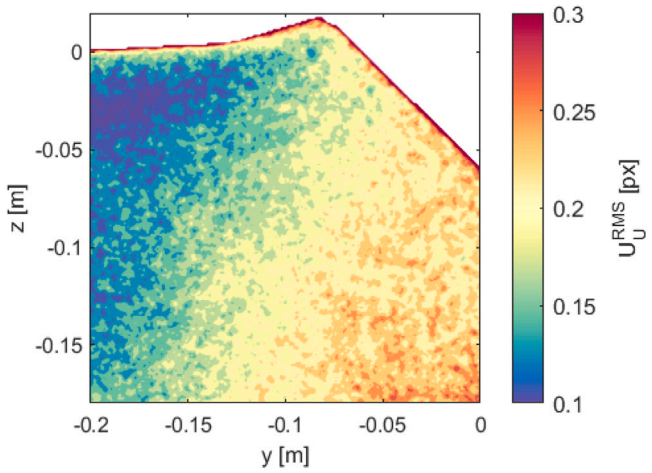

Fig. 11. Spatial variation of the RMS of the velocity field uncertainty at x=1.4 m.

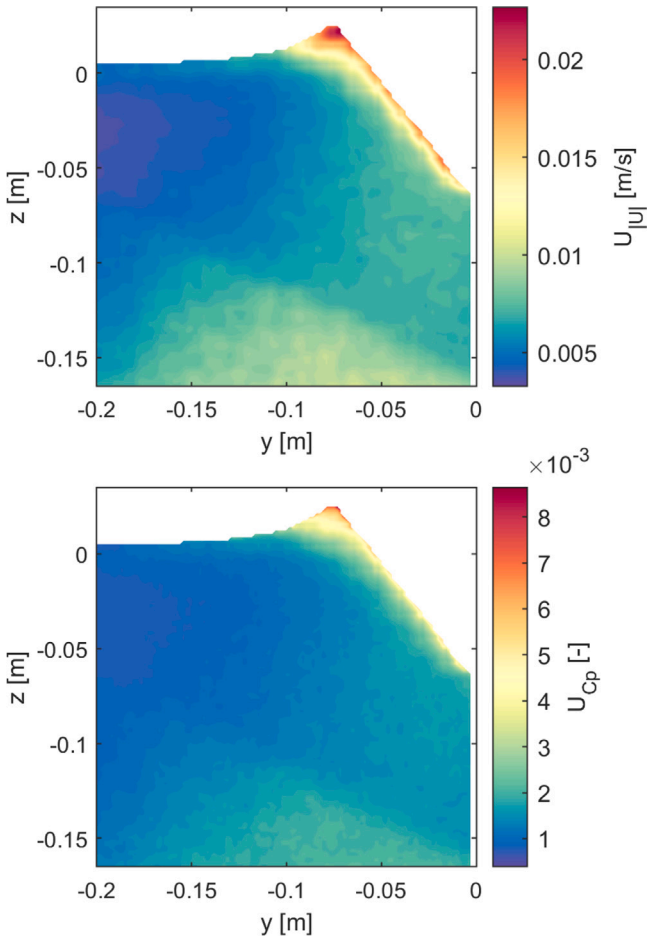

Fig. 12. Spatial variation of the uncertainty of the mean velocity magnitude (top) and the uncertainty of the pressure coefficient (bottom) at x=1.4 m.

8. Numerical simulations

To obtain a data set that can be used for comparison of the measured velocity field and the derived pressures, CFD simulations are performed with the open-source code OpenFOAM 6.0. Simulations are conducted for the calm water conditions with the model set to a fixed trim and sinkage, as well as for the forced heave oscillations. For the solution

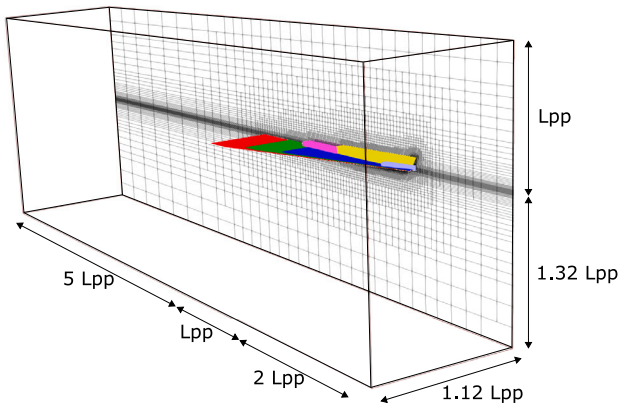

Fig. 13. Computational domain.

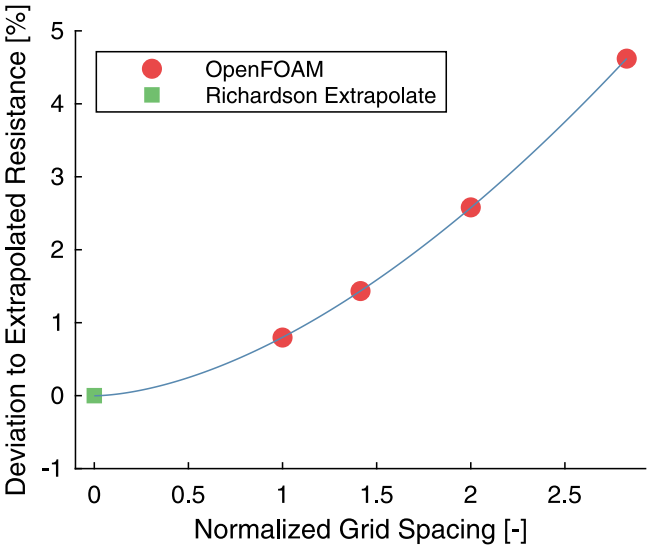

Fig. 14. Grid convergence study: Total resistance of grids with systematically varied grid refinement and extrapolated resistance value at zero grid spacing.

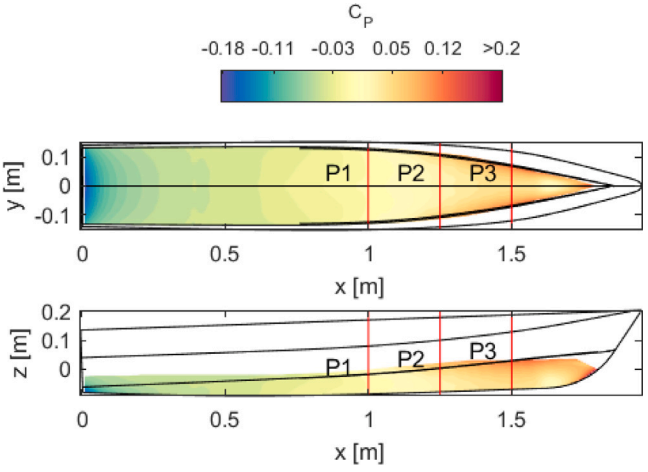

Fig. 15. Pressure distribution of the ship hull at Fr=0.8.

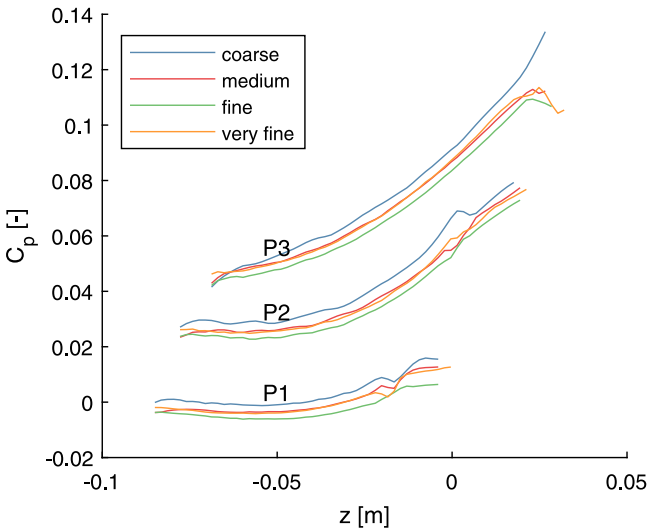

Fig. 16. Comparison of local pressure distribution of different numerical grids at x=1 m, 1.25 m and 1.5 m.

of both problems, the two-phase transient solver interFoam is chosen to solve the incompressible unsteady Reynolds-Averaged Navier–Stokes equations. These are discretized with second-order accuracy. For turbulence modeling, the k-omega-SST model is used. The numerical grid is generated with the hexahedral mesh generator snappyHexMesh. The meshing procedure is modified to allow for higher aspect ratio cells in the free-surface region and along the ship hull. The main dimensions of the numerical domain are chosen to fit the dimensions of the TU Delft towing tank, which is 2.44 m wide and 2.50 m deep. The position of the inlet and outlet are chosen according to the ITTC guidelines to prevent wave reflections. Due to the symmetry of the model, only one half of the ship model is meshed, to reduce the overall cell count and reduce simulation time. An overview of the domain, with all major dimensions, is given in Fig. 13, including an indication of the different refinement regions for the wake and bow wave.

For determination of the optimal mesh size and for a proof of the grid independence of the final solution, a grid convergence study is conducted with a total of 4 meshes. During the systematic refinement of the numerical grid, the cell count is varied from 337,542 up to 2,291,617 cells. For the finest mesh, the target cell size of the smallest cells outside the boundary layer is specified as $Lpp/1000$, with Lpp being the length between perpendiculars at floating position. Choosing a grid refinement ratio of $r = \sqrt{2}$, the coarser meshes are generated, resulting in an edge length of $Lpp/353$ of the smallest cell outside the boundary layer for the coarsest mesh. The boundary layer is designed for all meshes to yield a dimensionless wall distance y^+ of 30 for the cell closest to the wall, which enables the correct application of wall functions for modeling of the flow in the near-wall region. The growth ratio for the boundary layer cells is chosen as 1.2. Results of the grid refinement study are shown in Fig. 14, where the total resistance for all four meshes is plotted over their normalized grid spacing. The ship's speed selected for the refinement study is 3.32 m/s, which is equal to Fr=0.8. The resulting average y^+ value is within the range between 32 and 36 for all meshes. While the red dots indicate the total resistance from the CFD simulations, the green square shows the Richardson extrapolate, which gives an estimate of the total resistance at zero grid spacing. While the grid refinement ratio is constant, the order of convergence is determined with the solutions from the three finest grids $f_{1..3}$:

$$p = \frac{R_T(1) - R_T(\sqrt{2})}{R_T(\sqrt{2}) - R_T(2)} / \ln(r) \tag{10}$$

The determined order of convergence for these grids is 1.7. This value is used for the calculation of the extrapolated solution at zero grid spacing which is:

$$Pr_{h=0} = R_T(1) + (R_T(1) - R_T(\sqrt{2}))/(2^p - 1) \tag{11}$$

The total resistance is used as an initial indicator for grid independence. However, for the comparison with PIV measurements, the pressure distribution in the bow region is of greater interest. Fig. 15 gives an overview of the hydrodynamic pressure distribution on the ship hull for the finest mesh at Fr=0.8, showing the high-pressure regions at the front of the bow and within the bow wave. For the investigation of the influence of the grid on the pressure distribution on the ship hull, the hydrodynamic pressures are evaluated at three different sections $P1$, $P2$, $P3$, whose position is indicated in Fig. 15. In Fig. 16, the hydrodynamic pressure coefficient Cp on these sections is plotted over the height of the ship hull for all four grids with different refinement levels. For the three finest meshes, a good overall agreement can be found, with only minor differences. The pressure distribution obtained with the coarse grid, however, shows larger deviations in the region close to the chines. While the previously analyzed resistance monotonically converges with grid refinement level, the analysis of the local pressure distribution shows a fluctuation of the hydrodynamic pressures within a narrow band. Eventually, the finest mesh is chosen to be used for the calm water simulations. For the simulations with forced oscillations of the ship model, the medium-sized mesh is used to reduce the computational costs of the transient simulations.

9. Discussion and comparison of experimental and numerical results

For the final evaluation of the quality of the measured pressure fields, results from the PIV measurements are compared to the previously obtained numerical results. While the pressure field is reconstructed from the measured velocities with the help of the Poisson equation, velocity fields are compared first, to ensure that the experimental conditions match with those of the numerical simulations. Subsequently, reconstructed pressure fields and force distributions on the ship hull are compared.

9.1. Multi-plane PIV measurements

9.1.1. Velocity fields

Fig. 17 shows a comparison of the measured velocity field with numerical results at two selected slices of the volumetric velocity field, located at x=1.4 m and z=-0.01 m.

While the overall velocity distribution matches well for all three velocity components, significant local differences can be found. One of the most significant differences can be found by looking at the out-of-plane velocity field U_x. While the numerical solution resolves the flow within the boundary layer, it is not captured in the PIV measurement. The reason for this is twofold: For a successful pressure reconstruction, the domain needs to be sufficiently large. With a sensor size of 2048 x 2048 pixels and an interrogation window size of 24 pixels with an overlap of 75%, the spatial resolution was approximately 1 mm. This is about the same order of magnitude as the boundary layer thickness within this region. Additionally, reflections on the

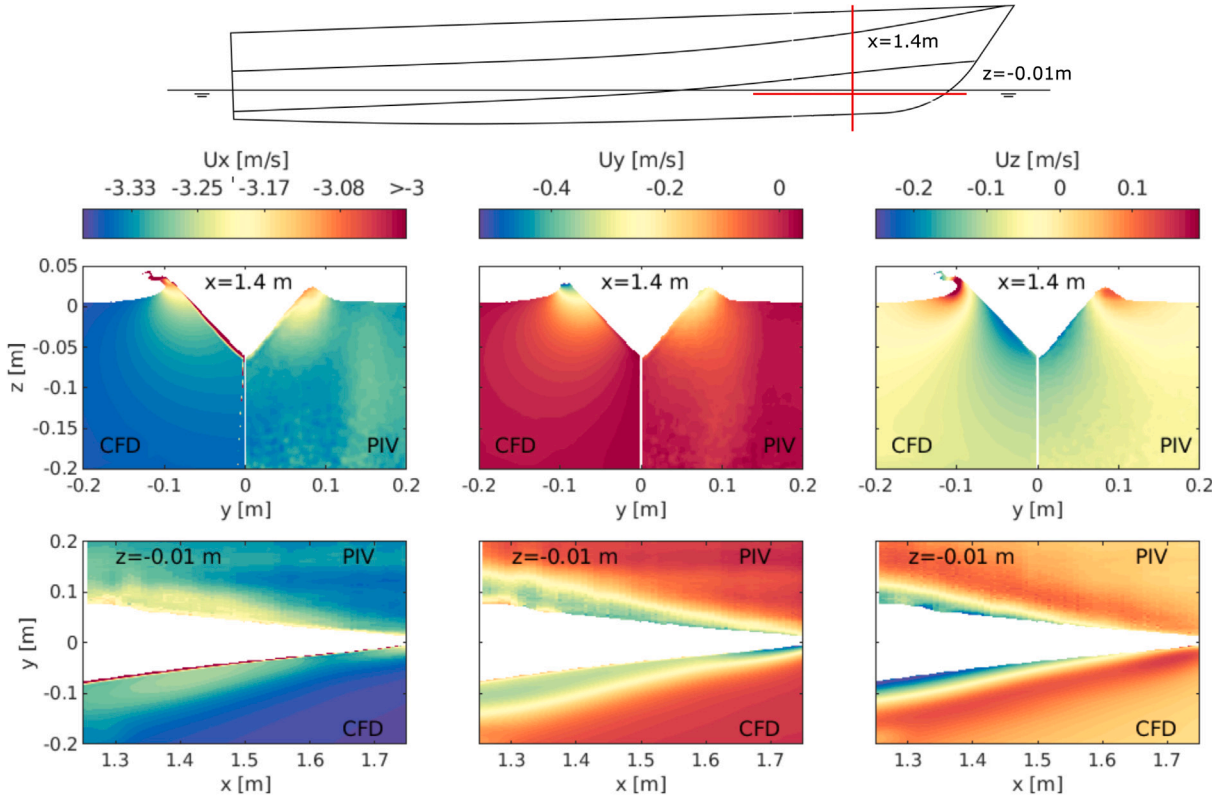

Fig. 17. Vertical and horizontal intersections of the volumetric velocity field at x=1.4 m (top) and z=-0.01 m (bottom). Comparison of experimental with numerical results.

model surface do not allow measurements in the direct vicinity of the surface. Further discrepancies are found within the spray root region and the jet, which is formed on the ship hull. With the current setup, it is not possible to obtain optical access to this region. Due to the limited spatial resolution, the high velocity gradient within this region is not sufficiently resolved. While the volumetric representation of the velocity field is generated only from vertical measurement planes which are perpendicular to the main flow direction, the horizontal slice of the domain is used to examine the continuity of the velocity field across the measurement planes. For all three velocity components, a smooth velocity field is observed along the x-direction. The overall comparison between both techniques shows good agreement, with the PIV technique capturing the main features of the flow. However, as already noticed, the near-wall flow cannot be captured with the PIV technique as a result of a compromise between spatial resolution and the size of the field of view. A quantitative comparison of experimental and numerical results is given in Fig. 18, where the in-plane velocity components at x=1.4 m are presented for three different horizontal lines at z=-0.01, −0.025 and −0.05 m. The experimentally obtained velocities include the propagated uncertainties. Based on these plots, it can be concluded that the experimental conditions were similar to the numerical simulations. Small deviations can be found for the horizontal velocity component U_y close to the ship hull.

9.1.2. Pressure fields and forces

With the volumetric description of the velocity field, the dynamic pressure field is reconstructed in the bow region of the ship model by solving the Poisson equation. The quality of the reconstructed pressure field is observed in Fig. 19 by comparison with the numerical results.

The pressure field is analyzed in three horizontal planes at z=-0.01, −0.03 and −0.05 m and 3 vertical slices at x = 1.4, 1.45 and 1.5 m. Comparing the pressure field within the two horizontal slices with numerical results shows that the main characteristics of the hydrodynamic pressure field are well reproduced with the pressure PIV technique. The high-pressure area within the bow wave, as well as the stagnation region close to the bow, can be found in the measurement results. Despite the absence of the boundary layer in the PIV measurements, good agreement between numerical and experimental results is found also close to the wall within the bow wave. However, close to the bow, the experimentally obtained pressure is lower than the numerically obtained pressure. Here, the high velocity gradient was not sufficiently captured by the PIV measurements, which had a limited spatial resolution. The pressure field in the vertical slices also shows good overall agreement between both methods. The limited optical access to the region of the jet which is formed on the ship hull and the limited spatial resolution results in an under prediction of the pressure peak within the spray root of the bow wave. A quantitative comparison of experimental and numerical results is given in Fig. 20, where the pressure coefficient at x=1.4 m is presented for three different horizontal lines at z=-0.01, −0.025 and −0.05 m. The experimentally obtained pressures include the propagated uncertainties from the performed Monte Carlo simulations. From these plots, it can be concluded that for large parts, the numerical results are within the uncertainty range of the experimental results. Small differences can be found close to the ship hull. To obtain the distribution of the hydrodynamic lift forces on the bow, the hydrodynamic pressures are interpolated to the ship hull. For the force integration, the region is split into sections of 0.01 m, which is equal to the spacing of the PIV measurement plane. The resulting sectional forces in the bow region and their uncertainties are presented in Fig. 21,

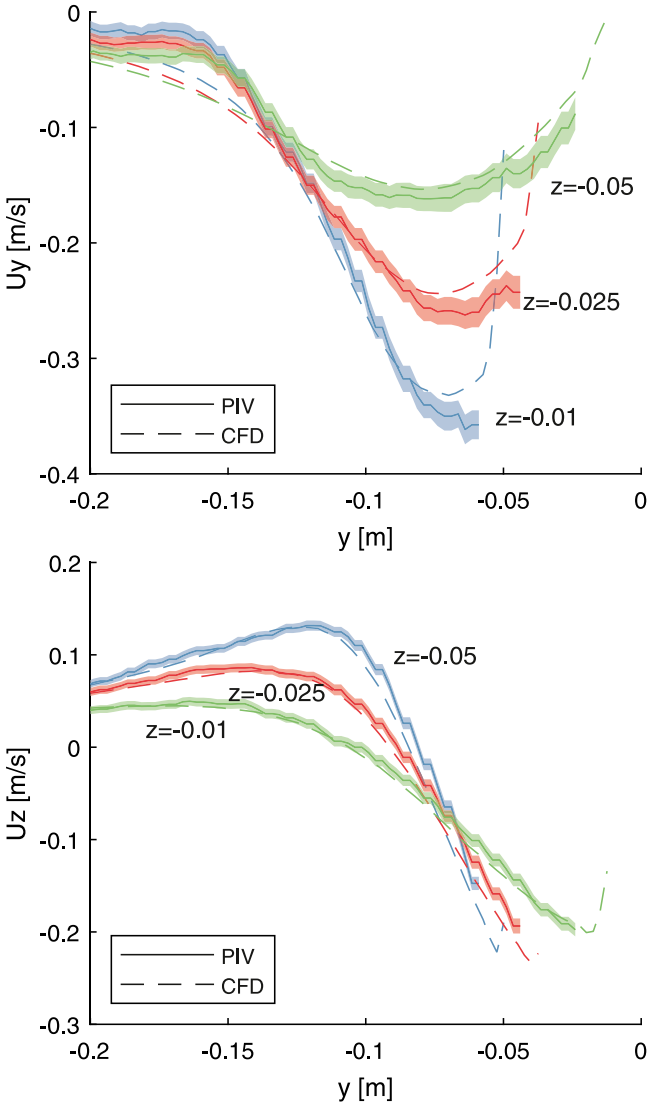

Fig. 18. In-plane velocity components at x=1.4 m along horizontal lines at z=-0.01, z=-0.025 m and z=-0.05 m. Comparison of experimental with numerical results.

where they are compared to the numerical results. The integration of the sectional forces leads to the total hydrodynamic lift force in the bow region. The experimentally obtained force is approximately 4% smaller compared to the CFD results. The distribution of sectional forces shows the largest differences between x=1.35 m and x=1.5 m. As already seen in Fig. 17, in this region the flow field within the bow wave is not fully captured due to limited optical access to the area above the spray root. Furthermore, the pressure peak in this region was underpredicted.

9.2. Oscillation tests

9.2.1. Velocity fields

Oscillation tests are performed at a lower carriage speed of 2.54 m/s, which is equal to Fr=0.6, and PIV recordings were obtained in three successive planes perpendicular to the main flow direction at x=1.35 m. Fig. 22 compares the experimentally obtained velocity fields with numerical results for two selected time instants during the downward motion. The two time instances are at 0.1 s within the downward acceleration phase and at 0.26 s where the model has reached its maximum downward velocity with the chine being immersed. The comparison with numerical results shows good overall agreement at both time instances. However, as already noticed during the multi-plane PIV measurements, the flow close to the ship hull is not resolved because of reflections, which did not allow measurements right at the wall, and the low spatial resolution. The latter and the limited optical access to the jet region, which forms on the ship hull, result in larger differences in this region. The largest differences for both cases are found at 0.26 s close to the immersed chines. As the forward speed of the model is reduced for the oscillation tests from 3.32 m/s to 2.54 m/s, by using the same maximum pixel displacement, the lower dynamic range of the velocities results in a higher resolution of this. However, while the numerical simulations capture the local acceleration of the flow around the sharp edge of the chine, this is not sufficiently captured by the PIV measurements.

9.2.2. Pressure fields and forces

The reconstructed pressure fields are presented in Fig. 23, where they are compared to the numerical results for three selected time-steps during the downward motion of the ship hull. While good agreement of both methods can be found for the velocity fields, differences become more pronounced in the pressure fields. In both, the numerical simulations, as well as the experiments, the high-pressure area increases during the downward motion. The pressure peak in the numerical results coincides with the immersion of the chine. However, in the PIV measurements it is shifted to a later time instance. Additionally, the pressure peak in the experimental results is not located at the hull-water intersection, as expected from the numerical simulation, but further shifted downwards. As already seen in the velocity field comparison, the numerical simulations were able to resolve the small local acceleration region above the edge of the chine. The effect of this can also be observed in the numerically observed pressure fields. However, as already noticed in the velocity fields, this effect is not captured with the experimental method. Fig. 24 shows the temporal evolution of the pressure distribution on the hull for one oscillation cycle at x=1.35 m. While the bottom line indicates the position of the keel, the upper line shows the position of the chine. The general behavior of the pressure field is well reproduced with the PIV measurements, showing a pressure increase during the downward motion and a low-pressure area during the upward motion. However, the difference already noticed in the sectional pressure field plots becomes clearer within the temporal evolution of the surface pressure distribution. The CFD results show a well-defined pressure peak when the chine becomes immersed, which is at 0.15 s. After once immersed, the peak pressure at the chine is reduced. The pressure peak, which is reconstructed from PIV experiments, is slightly shifted within time and space. Instead of capturing the high impact pressure on the chine, the high-pressure region is stretched over multiple time steps. Also captured in the CFD result, but not visible within the measured pressure field, is the pressure drop above the chine due to the acceleration of the flow in this region. The position of the low-pressure area during the upward motion is well predicted at approximately 0.6 s. However, PIV measurements indicate lower dynamic pressures compared to the numerical results. Fig. 24 (bottom) shows the time traces of the sectional forces obtained from the integration of the hydrodynamic pressure, including the propagated experimental uncertainties from the performed Monte Carlo simulations. While for the multi-plane PIV measurement, good agreement was found between CFD and experimental results, larger differences are found for the oscillation tests. In the numerical simulation, the hydrodynamic force rapidly increases up to the immersion of the chines. The experimental results, however, show a slow increase of force amplitude, which is in phase with the velocity field.

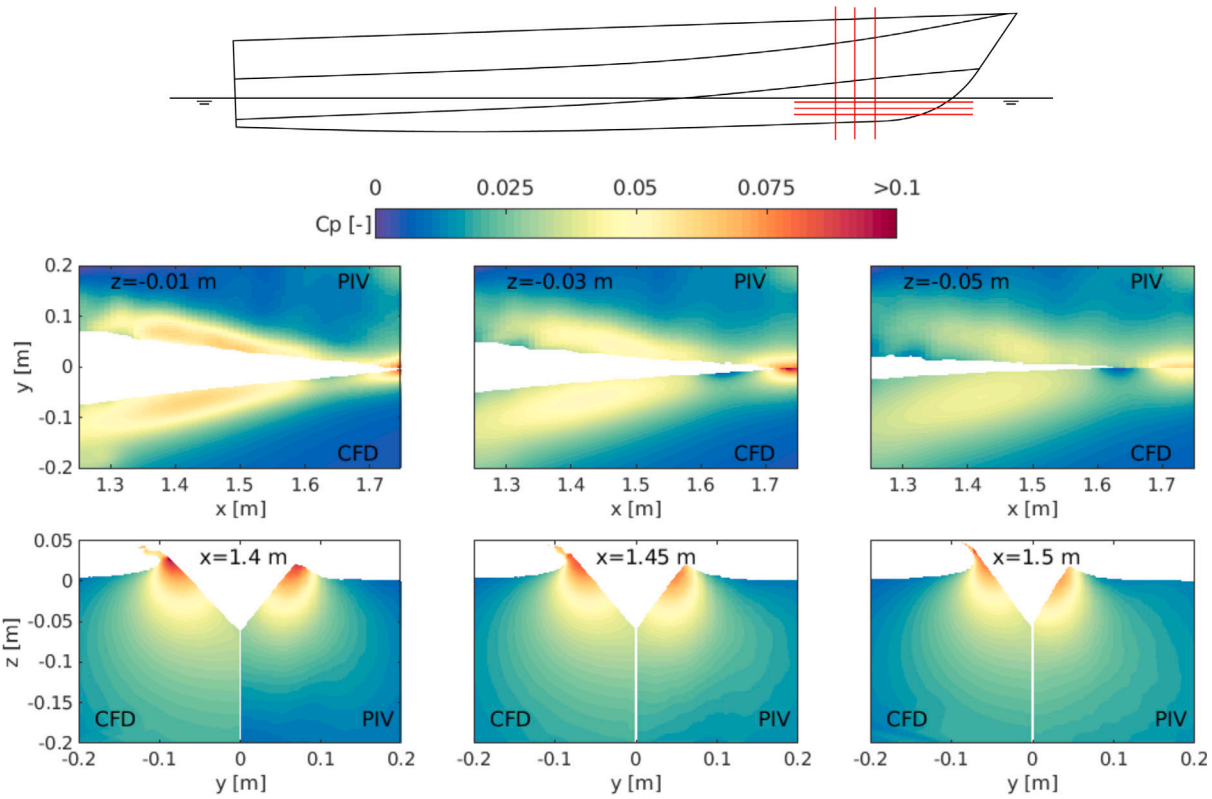

Fig. 19. Vertical and horizontal intersections of the time-averaged pressure field at z=-0.01, −0.03 and −0.05 m (top) and x = 1.4, 1.45 and 1.5 m (bottom). Comparison of experimental with numerical results.

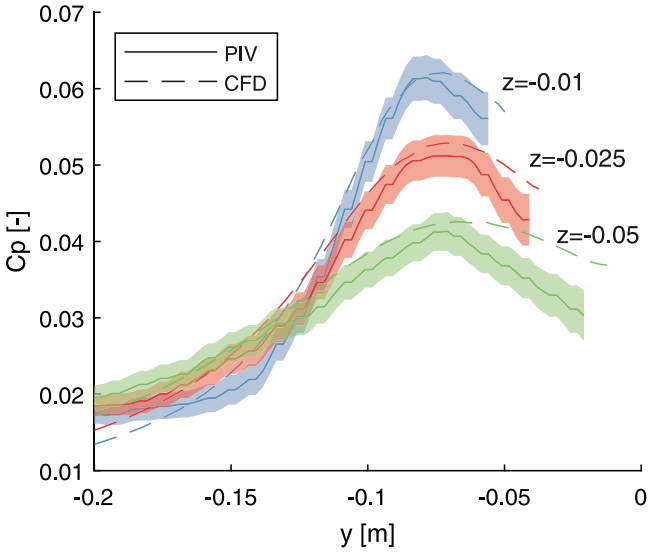

Fig. 20. Dynamic pressures at x=1.4 m along horizontal lines at z=-0.01, z=-0.025 m and z=-0.05 m. Comparison of experimental with numerical results.

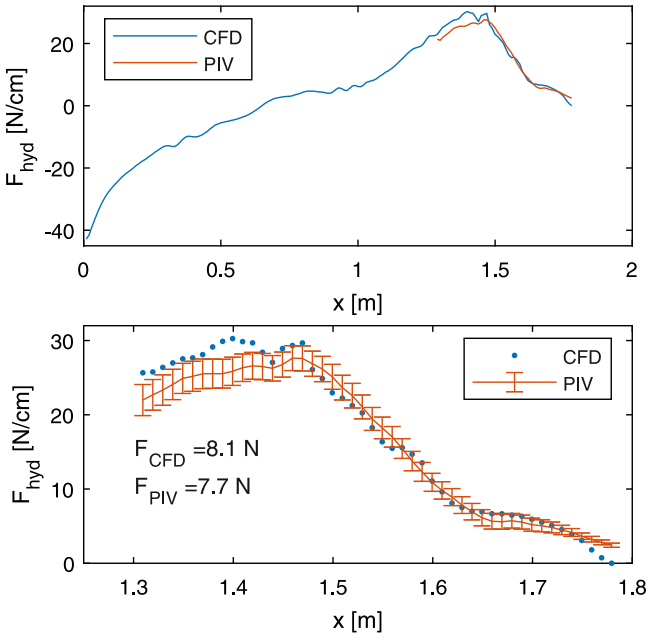

Fig. 21. Sectional force distribution in the bow region. Comparison of experimental with numerical results.

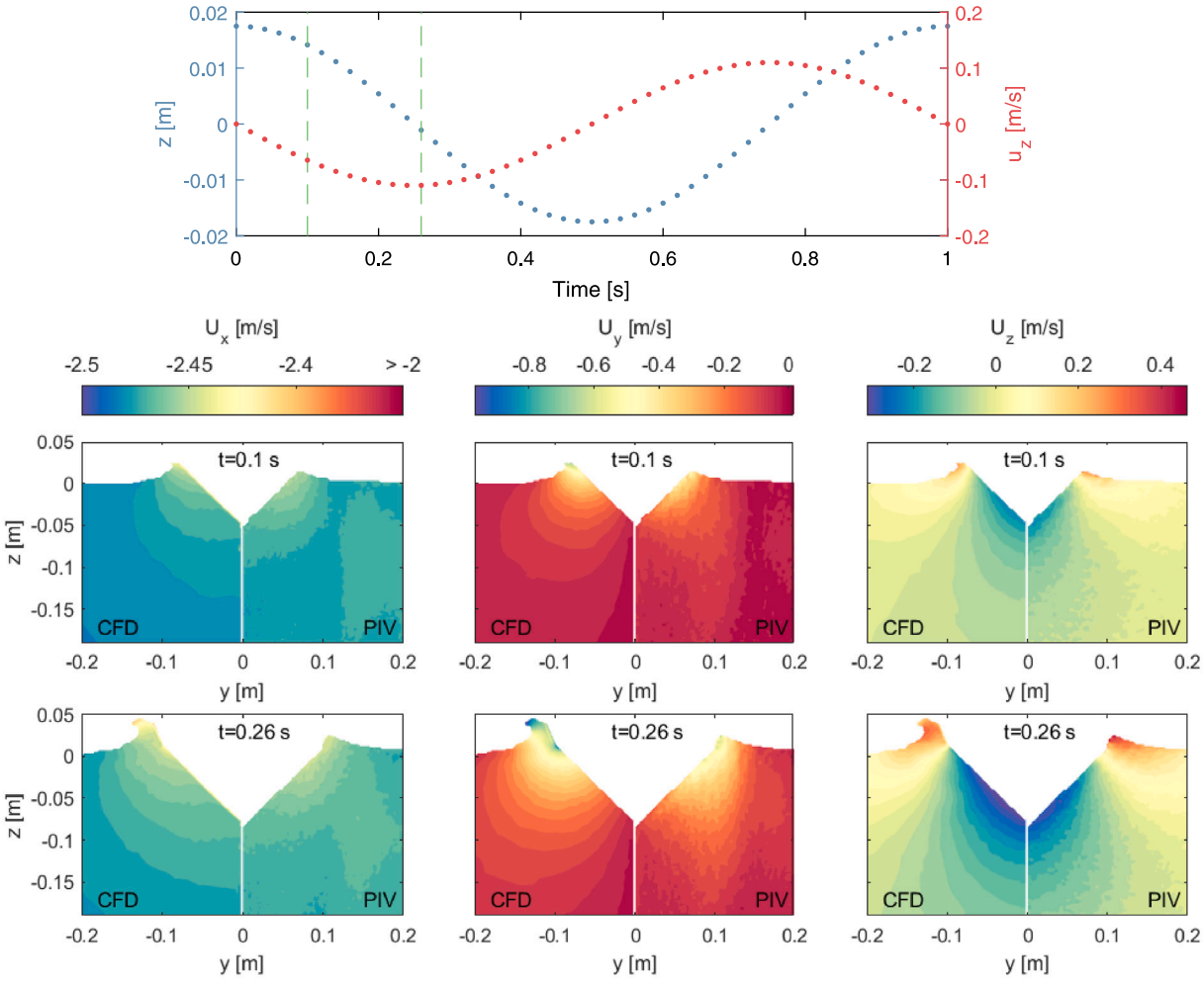

Fig. 22. Distribution of phase-averaged velocity fields at six selected time instants during the downward motion of the ship model, performing oscillatory motions at f=1 Hz with an amplitude of a=0.035 m. Comparison of experimental with numerical results.

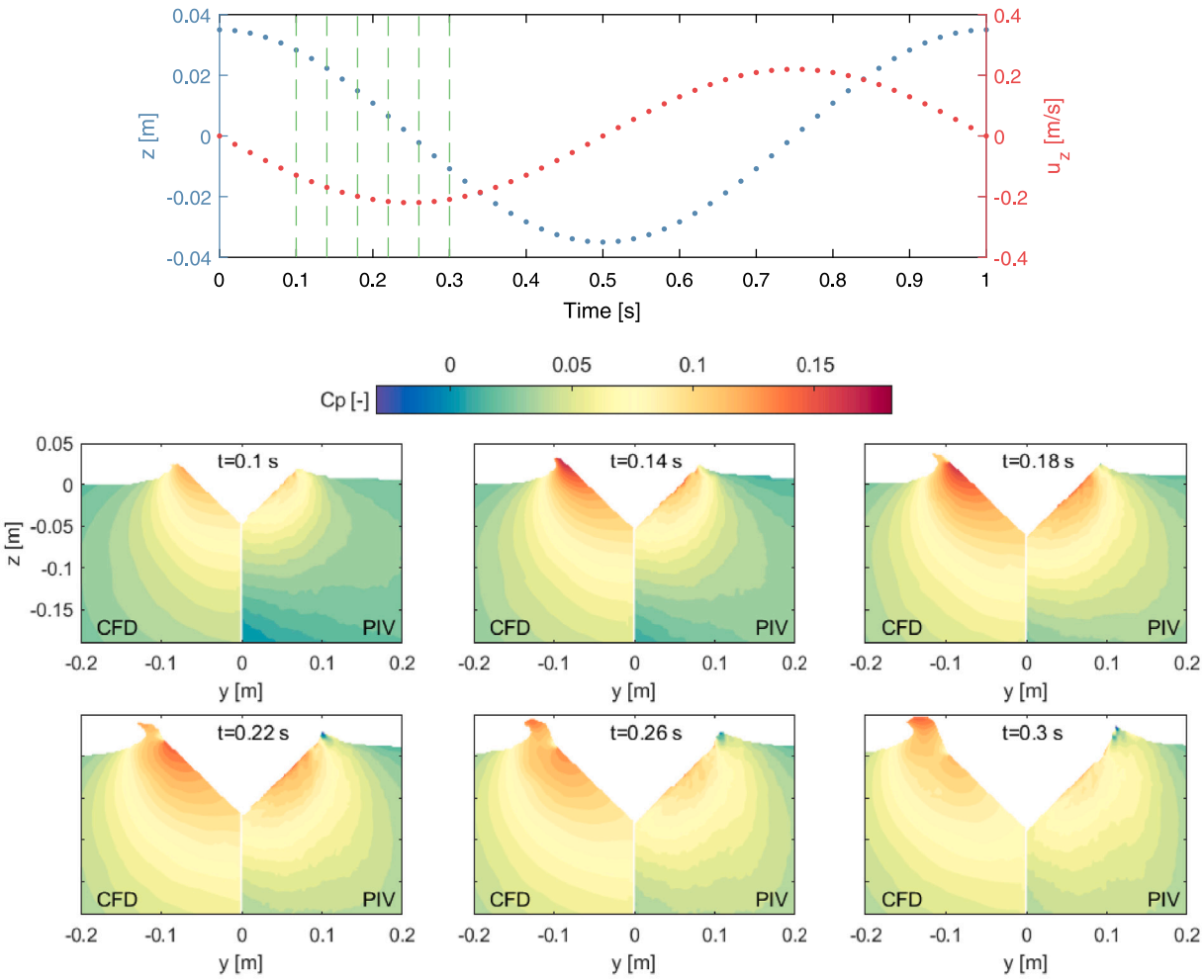

Fig. 23. Distribution of phase-averaged pressure fields at six selected time instants during the downward motion of the ship model, performing oscillatory motions at f=1 Hz with an amplitude of a=0.035 m. Comparison of experimental with numerical results.

10. Conclusions

In order to experimentally gain further insights into the hydrodynamics of high-speed ships, the PIV technique is applied for the analysis of the flow field in the bow region and a reconstruction of the hydrodynamic pressure field. In combination with the solution of the pressure Poisson equation, the PIV technique is tested as an alternative to existing pressure measurement techniques. Being a laser-optical measurement technique, the method requires optical access to the measurement region and good image quality of the particles. Limited optical access makes a measurement in the spray region of the bow wave impossible. Furthermore, reflections from the laser-sheet complicate measurements close to the hull surface.

The solution of the Poisson equation is dependent on adequate boundary conditions. If Dirichlet type boundary conditions are applied, a clear identification of boundaries is important. These can be the ship-hull but also the free surface. The identification of these is shown to be a non-trivial task. Especially the free surface cannot always be identified, which asks for intensive post-processing. However, it has been shown that the typical v-shaped bow sections of fast ships and the free surface with varying intensity can be automatically identified. While the method handles small free surface disturbances, the method needs to be further improved to handle larger disturbances, such as breaking waves.

The recorded flow fields are qualitatively and quantitatively compared with numerical simulations and the numerical results are found to be mostly within the uncertainty of the measurements. However, close to the ship hull larger deviations occur. Especially close to the chines the spatial resolution of the experimental methods needs to be improved in order to correctly capture the steep gradient in the velocity field. Considering the present study, the correct determination of the out-of-plane gradient, which is determined from multiple measurement planes, can be seen as one of the largest sources of uncertainty. While good results are obtained for the time-averaged multi-plane PIV measurements, larger deviations are found for the phase-averaged measurements, where the out-of-plane gradient has been determined from only three successive measurements. Additionally, the sampling frequency of the PIV system was limited to 50 Hz. With the studied flow being rather complex, a simpler test case is needed for a detailed evaluation of the influence of spatial and temporal resolution on the accuracy of the reconstructed pressure field.

In situations where traditional techniques cannot be applied, either due to the limited possibilities for fitting sensors or where their intrusiveness distorts the measurement result, the pressure PIV technique can be considered as an alternative, given that optical access to the observed region is provided. Additionally, when applied to volumetric representations of the flow field it has been shown that the technique can be used for the reconstruction of sectional pressure- and force-distributions on the ship hull.

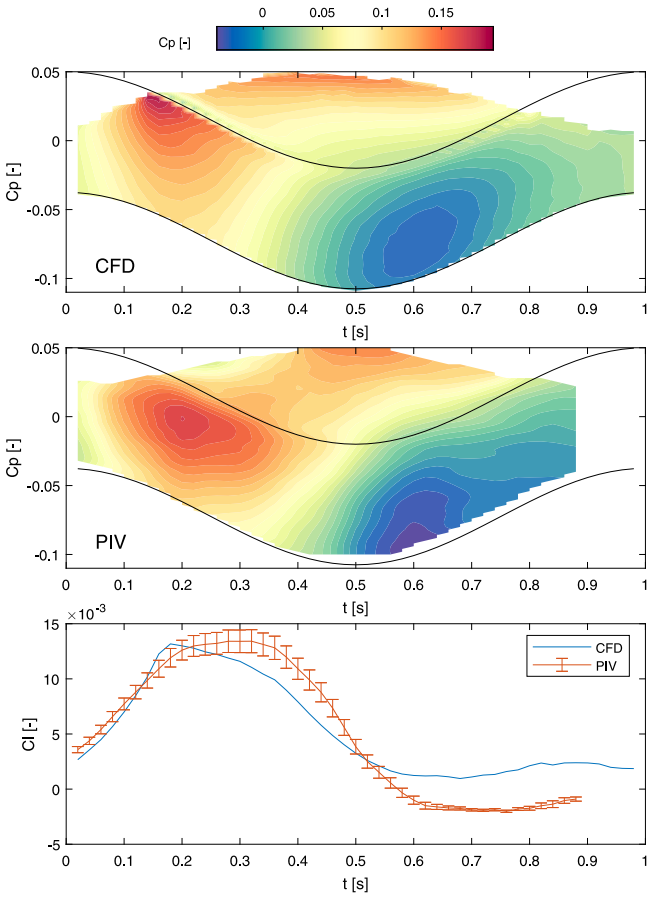

Fig. 24. Temporal evolution of the pressure distribution and lift coefficient on the ship hull at x=1.35 m for f=1 Hz and a=0.0175 m. Comparison of experimental with numerical results.

CRediT authorship contribution statement

G. Jacobi: Conceptualization, Methodology, Software, Investigation, Visualization, Writing. **C.H. Thill:** Supervision. **R.H.M. Huijsmans:** Supervision, Project administration.

Declaration of competing interest

The authors declare that they have no known competing financial interests or personal relationships that could have appeared to influence the work reported in this paper.

Acknowledgments

This publication is part of the project FastFem: Behaviour of Fast Ships in Waves, with project number 13266, which is partly financed by the Dutch Research Council (NWO).

References

Adrian, R.J., Westerweel, J., 2011. Particle Image Velocimetry. Cambridge University Press.

Albrecht, T., del Campo, V., Weier, T., Gerbeth, G., 2012. Comparison of PIV-based methods for airfoil loads evaluation. In: Symposium on Applications of Laser Techniques To Fluid Mechanics. No. July 2015. pp. 9–12.

Azijli, I., Sciacchitano, A., Ragni, D., Palha, A., Dwight, R.P., 2016. A posteriori uncertainty quantification of PIV-based pressure data. Exp. Fluids 57 (5), 1–15. http://dx.doi.org/10.1007/s00348-016-2159-z.

Baur, T., 1999. PIV with high temporal resolution for the determination of local pressure reductions from coherent turbulence phenomena. In: Proc. 3rd Int. Workshop on PIV-Santa Barbara. pp. 101–106.

Capone, A., Alves Pereira, F., Maiocchi, A., Di Felice, F., 2019. Analysis of the hull wake of a twin-screw ship in steady drift by Borescope Stereo Particle Image Velocimetry. Appl. Ocean Res. 92 (September), 101914. http://dx.doi.org/10.1016/j.apor.2019.101914.

De Jong, P., 2011. Seakeeping Behaviour of High Speed Ships: An Experimental and Numerical Study (Ph.D. thesis). Delft University of Technology.

De Kat, R., Van Oudheusden, B.W., Scarano, F., 2009. Instantaneous pressure field determination around a square-section cylinder using time-resolved stereo-PI. In: 39th AIAA Fluid Dynamics Conference. pp. 3–6. http://dx.doi.org/10.2514/6.2009-4043.

De Silva, C.M., Philip, J., Marusic, I., 2013. Minimization of divergence error in volumetric velocity measurements and implications for turbulence statistics. Exp. Fluids 54 (7), http://dx.doi.org/10.1007/s00348-013-1557-8.

Dong, R.R., Katz, J., Huang, T.T., 1997. On the structure of bow waves on a ship model. J. Fluid Mech..

Duda, R.O., Hart, P.E., 1971. Use of the Hough Transformation to Detect Lines and Curves in Pictures. Technical Report, Sri International Menlo Park Ca Artificial Intelligence Center.

Falchi, M., Felli, M., Grizzi, S., Aloisio, G., Broglia, R., Stern, F., 2014. SPIV Measurements around the DELFT 372 catamaran in steady drift. Exp. Fluids 55 (11), 1844. http://dx.doi.org/10.1007/s00348-014-1844-z.

Felis-Carrasco, F., Watz, B.B., Hess, D., Mendez, M.A., 2021. A study on PIV-based pressure measurements using CFD techniques.

van Gent, P.L., Michaelis, D., van Oudheusden, B.W., Weiss, P., de Kat, R., Laskari, A., Jeon, Y.J., David, L., Schanz, D., Huhn, F., Gesemann, S., Novara, M., McPhaden, C., Neeteson, N.J., Rival, D.E., Schneiders, J.F., Schrijer, F.F., 2017. Comparative assessment of pressure field reconstructions from particle image velocimetry measurements and Lagrangian particle tracking. Exp. Fluids 58 (4), 1–23. http://dx.doi.org/10.1007/s00348-017-2324-z.

Gui, L., Longo, J., Stern, F., 2001. Towing tank PIV measurement system, data and uncertainty assessment for DTMB Model 5512. Exp. Fluids 31 (3), 336–346. http://dx.doi.org/10.1007/s003480100293.

Haigermoser, C., 2009. Application of an acoustic analogy to PIV data from rectangular cavity flows. Exp. Fluids 47 (1), 145–157. http://dx.doi.org/10.1007/s00348-009-0642-5.

Huijsmans, R., Graham, M., Kendon, T., 2005. The flow around FPSO's in steep regular beam waves: Results of piv experiments and RANS computations. In: 24th International Conference on Offshore Mechanics and Arctic Engineering. American Society of Mechanical Engineers, pp. 965–972.

Jacobi, G., Thill, C.H., van't Veer, R., Huijsmans, R.H., 2019. Analysis of the influence of an interceptor on the transom flow of a fast ship by pressure reconstruction from stereoscopic scanning PIV. Ocean Eng. 181 (February), 281–292. http://dx.doi.org/10.1016/j.oceaneng.2019.02.062.

Jensen, A., Pedersen, G.K., 2004. Optimization of acceleration measurements using PIV. Meas. Sci. Technol. 15 (11), 2275–2283. http://dx.doi.org/10.1088/0957-0233/15/11/013.

Keuning, J., Toxopeus, S., Pinkster, J., 2001. The effect of bow shape on the seakeeping performance of a fast monohull. In: FAST Conference Proceedings.

Koschatzky, V., Westerweel, J., Boersma, B.J., 2010. Comparison of two acoustic analogies applied to experimental PIV data for cavity sound emission estimation. In: 16th AIAA/CEAS Aeroacoustics Conference (31st AIAA Aeroacoustics Conference). http://dx.doi.org/10.2514/6.2010-3812.

Lawson, N.J., Wu, J., 1997. Three-dimensional particle image velocimetry: Experimental error analysis of a digital angular stereoscopic system. Meas. Sci. Technol. 8 (12), 1455–1464. http://dx.doi.org/10.1088/0957-0233/8/12/009.

Liu, X., Katz, J., 2006. Instantaneous pressure and material acceleration measurements using a four-exposure PIV system. Exp. Fluids 41 (2), 227–240. http://dx.doi.org/10.1007/s00348-006-0152-7.

Liu, X., Katz, J., 2011. Time resolved PIV measurements elucidate the feedback mechanism that causes low-frequency undulation in an open cavity shear layer. In: 9th International Symposium on Particle Image Velocimetry. No. Sarohia 1977.

Longo, J., Shao, J., Irvine, M., Gui, L., Stern, F., 2001. Unsteady PIV for regular head waves. Lcgui.Net 5512.

Longo, J., Shao, J., Irvine, M., Stern, F., 2007. Phase-averaged PIV for the nominal wake of a surface ship in regular head waves. J. Fluids Eng. 129 (5), 524. http://dx.doi.org/10.1115/1.2717618.

Nila, A., Vanlanduit, S., Vepa, S., Van Paepegem, W., 2013. A PIV-based method for estimating slamming loads during water entry of rigid bodies. Meas. Sci. Technol. 24 (4), http://dx.doi.org/10.1088/0957-0233/24/4/045303.

Otsu, N., 1979. A threshold selection method from gray-level histograms. IEEE Trans. Syst. Man Cybern. 1, 62–66.

van Oudheusden, B.W., 2013. PIV-Based pressure measurement. Meas. Sci. Technol. 24 (3), http://dx.doi.org/10.1088/0957-0233/24/3/032001.

Pröbsting, S., Scarano, F., Bernardini, M., Pirozzoli, S., 2013. On the estimation of wall pressure coherence using time-resolved tomographic PIV this article is part of the topical collection on application of laser techniques to fluid mechanics 2012. Exp. Fluids 54 (7), http://dx.doi.org/10.1007/s00348-013-1567-6.

Ragni, D., Oudheusden, B.W.V., Scarano, F., 2012. 3D pressure imaging of an aircraft propeller blade-tip flow by phase-locked stereoscopic PIV. pp. 463–477. http://dx.doi.org/10.1007/s00348-011-1236-6.

Regert, T., Chatellier, L., Tremblais, B., David, L., 2011. Determination of pressure fields from time-resolved data. In: 9th International Symposium on Particle Image Velocimetry. No. July. pp. 1–5.

Savitzky, A., Golay, M.J., 1964. Smoothing and differentiation of data by simplified least squares procedures. Anal. Chem. 36 (8), 1627–1639.

Schanz, D., Schröder, A., Gesemann, S., Michaelis, D., Wieneke, B., 2013. ' Shake The Box ': A highly efficient and accurate Tomographic Particle Tracking Velocimetry (TOMO-PTV) method using prediction of particle positions. In: 10th International Symposium on Particle Image Velocimetry - PIV13. Delft, the Netherlands, July 1-3. pp. 1–13.

Schneiders, J.F., Caridi, G.C., Sciacchitano, A., Scarano, F., 2016. Large-scale volumetric pressure from tomographic PTV with HFSB tracers. Exp. Fluids 57 (11), 1–8. http://dx.doi.org/10.1007/s00348-016-2258-x.

Sciacchitano, A., Wieneke, B., 2016. PIV Uncertainty propagation. Meas. Sci. Technol. 27 (8), http://dx.doi.org/10.1088/0957-0233/27/8/084006.

Van Oudheusden, B.W., L., 2007. Principles and application of velocimetry-based planar pressure imaging in compressible flows with shocks. In: 7th Int. Symp. on PIV. Rome, Italy. pp. 11–14.

Wang, Z., Gao, Q., Pan, C., Feng, L., Wang, J., 2017. Imaginary particle tracking accelerometry based on time-resolved velocity fields. Exp. Fluids 58 (9), http://dx.doi.org/10.1007/s00348-017-2394-y.

Wieneke, B., 2015. PIV Uncertainty Quantification from Correlation Statistics. IOP Publishing, http://dx.doi.org/10.1088/0957-0233/26/7/074002.